Title	Applicability of extended modified Archimedes' law to various granular and intruder properties
Author(s)	Iikawa, Naoki; Katsuragi, Hiroaki
Citation	Computational Particle Mechanics. 2025
Version Type	VoR
URL	https://hdl.handle.net/11094/102740
rights	This article is licensed under a Creative Commons Attribution 4.0 International License.
Note	

Computational Particle Mechanics
https://doi.org/10.1007/s40571-025-01025-9

Applicability of extended modified Archimedes' law to various granular and intruder properties

Naoki Iikawa[1,2] · Hiroaki Katsuragi[1]

Received: 30 January 2025 / Revised: 22 June 2025 / Accepted: 27 June 2025

Abstract

Although resistive force during intruder penetration into granular layers plays a crucial role in various applications, its underlying mechanisms remain insufficiently understood. In this study, we investigate penetration resistive force using discrete element simulations, systematically varying the angle of repose, interparticle cohesion stress, intruder shape (tip angle and horizontal cross-sectional geometry), and the interface friction between the intruder and particles. The simulation results are then compared with estimations from the extended modified Archimedes' law. As a result, the current model cannot fully capture the effects of these factors, except for intruder shape. Through the detailed strain field analysis of granular layer during intruder penetration, we identify that the discrepancy between the model and simulation results arises from differences in the failure modes of the granular layer. To address this, we modify the model parameters based on the failure modes. Furthermore, we introduce a formula that incorporates the effect of the interface friction, which is not accounted for in the current model. With these modifications, the model can quantitatively estimate penetration resistive forces in dry and cohesive granular layers across various simulation conditions. The analysis of variance indicates that the interface friction and angle of repose have a significant impact on prediction accuracy of the model, supporting the effectiveness of the modification. This study offers a comprehensive understanding of the key factors influencing penetration resistive forces and contributes to the development of more accurate predictive models.

Keywords Granular materials · Discrete element modeling · Stress analysis · Shallow penetration

Abbreviations

β	Tip angle of stagnant zone
χ	Shape parameter of particle
Δt	Timestep in the simulation [s]
Δx	Coefficient of distance which the attraction force continues after particles detouch
$\delta_{\theta ri}, \delta_{\theta si}$	total relative rolling and twisting angular displacements from particle j to i
δ_{nij}	Normal overlap or distance between particle particles i and j
$\dot{\gamma}$	Shear strain rate [s^{-1}]
γ_n, γ_t	normal and tangential viscous dampings [kg/s]
μ	Sliding friction coefficient
μ_{gg}	Sliding friction coefficient between particles
μ_{og}	Sliding friction coefficient between intruder and particle
ω_{ri}, ω_{si}	relative rolling and twisting angular velocities from particle j to i [s^{-1}]
ϕ	Angle of repose [deg]
ρ_g, ρ_o	densities of particle and intruder [kg/m^3]
Θ	Tip angle of intruder [deg]
C	Cohesive stress parameter in DEM [Pa]
C'	Model cohesive stress [Pa]
d_m	Mean particle diameter [m]
F_c^j	Cohesive force from adjacent particle j [N]
F_n^j, F_t^j	normal and tangential forces between particle i and j [N]
F_p	Penetration resistive forces [N]
$F_{p,DEM}$	F_p obtained from the simulation [N]
$F_{p,model}$	F_p computed from the model [N]
g	Gravitational acceleration [m/s^2]

✉ Naoki Iikawa
naoki_iikawa@global.komatsu

Hiroaki Katsuragi
katsuragi@ess.sci.osaka-u.ac.jp

[1] Department of Earth and Space Science, The University of Osaka, 1-1 Machikaneyama, Toyonaka, Osaka 560-0043, Japan

[2] Development Division, Komatsu Ltd., 3-25-1 Shinomiya, Hiratsuka, Kanagawa 254-8555, Japan

Published online: 23 July 2025

I_i	Moment of inertia of particle i [kg/m^2]
k	Slope calculated by the linear regression on $F_{p,model}$ and $F_{p,DEM}$
k_n, k_t	normal and tangential spring constants [kg/s^2]
K_c, K_ϕ	coefficients of cohesion-derived and friction-derived forces
l	Base length of intruder[m]
l_c	Constant length of intruder [m]
l_p	Penetrated base length of intruder [m]
m_i	Mass of particle i [kg]
M_r^j, M_s^j	rolling and twisting moments from particle j to i [Nm]
R	Radius of cone[m]
r^*	Effective radius [m]
r_i, r_j	radii of particle i and j [m]
r_i^j	Vector from the center of particle i to the contact point with particle j [m]
S_p	Penetrated horizontal cross-section area of a intruder [m^2]
v_i	Velocity of particle i [m/s]
V_p	Penetrated volume of a intruder [m^3]
v_p	Penetration velocity [m/s]
z_p	Penetration depth [m]

1 Introduction

In the fields of civil engineering, biology, and planetary sciences, researchers and engineers have recently focused on the penetration resistive forces (F_p) experienced by an intruder penetrating granular materials at relatively shallow depths (approximately 2–5 times the intruder's diameter). For example, in civil engineering, the estimation of F_p in soil ground has potential applications for optimizing the configurations and operations of machinery in excavation, transportation, and locomotion on soil surfaces [1–11]. In biology, understanding F_p in soil has been used to explain the morphology of organisms adapted for penetration into sandy environments [12–15]. Additionally, biomimetic studies have aimed to improve penetration mechanisms by mimicking evolutionary adaptations in organism shapes [16–18]. In planetary sciences, F_p in regolith contributes to understanding impact crater formation processes, spacecraft landings on asteroids and solid planets, and rover design and development [19–24]. Recent studies have also tried to estimate the mechanical properties of soil and regolith through in situ measurements of F_p [25, 26]. Thus, understanding F_p acting on an intruder is not only of fundamental physical interest but also crucial for numerous practical applications.

Over the past decades, extensive studies have investigated the penetration and impact of intruders into granular layers and proposed several analytical models to quantitatively estimate F_p [2, 27–35]. In these studies, Katsuragi and Durian [29] proposed a simple analytical model analogous to Poncelet's force law, based on a series of experiments involving sphere impacts on granular layers. This phenomenological model expresses F_p as the sum of a force linearly proportional to the hydrostatic-like penetration depth, derived from granular friction, and an inertial force proportional to the square of the velocity. The validity of this model has been supported by numerous subsequent experimental and simulation studies [22, 30, 36]. Granular Resistive Force Theory (RFT), a model used to calculate forces acting on each small surface element of a penetrating intruder, has also been proposed to estimate F_p for complex intruder shapes [2, 34]. RFT relies on the assumption that F_p is linearly proportional to depth in shallow regions of granular layers. By combining RFT with multibody dynamics, it has been employed to predict the behavior of robots and tires on granular surfaces [2, 4, 9]. More recently, Kang et al. [31] and Feng et al. [32] proposed the Modified Archimedes' Law Theory (MALT) model, which is based on slip-line field analysis during intruder penetration, assuming that the granular layer behaves as a continuum—a concept long studied in geotechnical engineering [27, 28, 37, 38]. In the MALT model, F_p is expressed as the product of the penetration volume, the bulk density of the granular layer, gravitational acceleration, and a coefficient depending solely on the granular friction angle (equal to the angle of repose, ϕ). The key advantage of the MALT model is that F_p can be calculated exclusively from the physical properties of the granular layer and the penetrated volume of the intruder. Subsequent studies have suggested that the MALT model is also applicable under microgravity conditions and when the penetration velocity exceeds the quasi-static regime [39–41].

One of the key challenges in applying these models to estimate F_p for real granular materials is addressing cohesion arising from water or clay components between particles. Granular materials found on the surfaces of the Earth and solid planets generally exhibit cohesive properties [19, 23, 42–45]. It is difficult to estimate F_p for such cohesive granular layers by directly applying the previous models, which have primarily been developed for dry conditions. Therefore, it is essential to model F_p while accounting for the interaction between an intruder and cohesive granular layers. Recent studies have investigated F_p in cohesive granular layers through both experiments and simulations [22, 24, 25, 46–48]. For instance, Sharpe et al. [46], Brzinski et al. [47], and Zhang et al. [48] have demonstrated that increased interparticle cohesive stress reduces the penetration depth of intruders and animals. Moreover, Bagheri et al. [24] and Cheng et al. [25] reported that higher water content and increased interparticle cohesive stress result in larger F_p. These studies, either directly or indirectly, indicate a correlation between F_p and cohesion. Furthermore, phenomenological models for F_p in cohesive granular layers have been proposed in recent years. For instance, some models suggest that F_p is proportional to the interparticle cohesive stress [22, 25]. We have also extended the MALT model to address cohesive granular layers [49]. Our findings reveal that the extended MALT model can estimate F_p using only ϕ and the bulk cohesive stress.

However, previous studies related to the MALT model have assumed simplified problem settings. Thus, the applicability of the model in complex settings remain insufficiently explored. For instance, while the individual effects of tip angle and horizontal cross-sectional geometry on F_p have been investigated [31, 33, 50, 51], their simultaneous effects have not been examined. Additionally, Meyerhof [27], Vesić [28], Xi et al. [52] have shown that F_p is affected by the interface friction between the intruder and particles. However, this effect is not currently incorporated into the MALT model, and its inclusion is necessary for more accurate F_p estimation. Regarding the effect of granular properties on F_p, previous studies have explored the influence of ϕ [32, 35]. Nevertheless, the appropriate values of the bulk cohesive stress used in the model have not been adequately discussed. In particular, in the fields of planetary science and terramechanics, the behaviors of regolith and soil, which are difficult to reproduce through experiments, are often investigated using simulations [7, 22]. Therefore, it is crucial to clarify how measurable and definable quantities in actual soil and simulation correspond to the parameters of the extended MALT model.

In this study, we investigate F_p by varying the tip angle, horizontal cross-sectional geometry, and interface friction of intruders for dry and cohesive granular materials with different ϕ using discrete element method (DEM) simulations. The simulated F_p is compared with the predicted value in the extended MALT and used to evaluate the prediction accuracy of the model. Subsequently, we examine the influences not considered in the current model, the failure mode and interface friction. Furthermore, we incorporate these effects into the model. Finally, we evaluate the improvement in the prediction accuracy caused by these modifications. We also discuss the factors that have a significant impact on the prediction accuracy of the model.

2 Numerical and theoretical study

2.1 Numerical study

2.1.1 Discrete element method

To investigate the influence of various granular and intruder properties on F_p, we perform intruder penetration simulations using DEM. As the simulation platform, we use an open-source DEM engine, LIGGGHTS(R)-PUBLIC Version 3.8.0 [53, 54]. Details on the applicability of the adopted model to dry and cohesive granular materials, including comparisons with experiments, are described in our previous study [49]. Thus, this section provides an overview of the adopted DEM model.

We basically employ the Hertz–Mindlin contact model, the rolling resistance model [55], and cohesive bond force model [1], respectively. The motion equations for the translational and rotational directions of the particle i are expressed by the following equations:

$$\begin{aligned} m_i \frac{dv_i}{dt} &= \sum (F_n^j + F_t^j + F_c^j) + m_i g, \\ I_i \frac{d\omega_i}{dt} &= \sum (r_i^j \times F_t^j + M_r^j + M_s^j), \end{aligned} \tag{1}$$

where m_i, v_i, I_i, and ω_i are the mass, translational velocity, moment of inertia, and angular velocity of particle i, respectively; r_i^j is the vector from the center of particle i to the contact point with particle j; g is the gravitational acceleration ($g = 9.8$ m/s^2); and the symbol $\sum$ denotes the sum of all forces or moments acting on particle i from adjacent particles. For the normal and tangential forces between contacting particles i and j, F_n^j and F_t^j, these fully follow the Hertz model in LIGGGHTS [54].

M_r^j and M_s^j are the rolling and twisting moments between contacting particle i and j due to rolling resistance, respectively. Each moment is described as follows:

$$\begin{aligned} M_r^j &= \min \left[0.525 |F_n^j| \chi r^*,\ 0.25 (\chi r^*)^2 (k_n \delta_{\theta r i} + \gamma_n \omega_{ri}) \right], \\ M_s^j &= \min \left[0.65 \mu |F_n^j| \chi r^*,\ 0.5 (\chi r^*)^2 (k_t \delta_{\theta s i} + \gamma_t \omega_{si}) \right], \end{aligned} \tag{2}$$

where k_n, k_t, γ_n, and γ_t are the normal spring constant, the tangential spring constant, the normal viscous damping coefficient, and the tangential viscous damping coefficient, respectively; $\delta_{\theta ri}$, $\delta_{\theta si}$, ω_{ri}, and ω_{si} are the total relative rolling angular displacement, the total relative twisting angular displacement, the relative rolling angular velocity, and the relative twisting angular velocity, in the contact of particles i and j, respectively; r^* is effective radius; χ is a dimensionless shape parameter that adjusts the rotational resistance due to the irregularity of the actual particle shape; and μ is sliding friction coefficient between particles or between a particle and an intruder surface. The symbol "min" denotes choice of the smaller of the two values in parentheses.

F_c^j is the attraction force from adjacent particle j to particle i due to cohesive stress between particles. This force is described as follows:

$$F_c^j = \begin{cases} -\frac{C}{\mu_{gg}} (r_i + r_j)^2 & : \text{if } \delta_{nij} \geq 0, \\ -\frac{C}{\mu_{gg}} (r_i + r_j)^2 \left(1 + \frac{\delta_{nij}}{\Delta x (r_i + r_j)}\right) & : \text{if } \delta_{nij} < 0, \text{ separation}, \\ 0 & : \text{if } \delta_{nij} < 0, \text{ approach}, \end{cases} \tag{3}$$

where C is cohesive stress parameter representing the degree of attraction force between particles i and j; μ_{gg} is the friction coefficient between particles i and j; r_i and r_j are respective radii of contacting particles i and j; Δx is coefficient of distance which the attraction force continues after particles detouch, and $\Delta x = 0.1$ is used in this study; and δ_{nij} is normal overlap or distance between particle particles i and j. In other words, δ_{nij} represents the amount of overlap between two particles if it is positive, and the distance between particle surfaces if it is negative.

2.1.2 DEM parameters

The DEM parameters for each granular type are presented in Table 1. Here, regardless of the granular type, Young's modulus E, Poisson ratio ν, coefficient of restitution e, particle density ρ_g, and intruder density ρ_o are set to 1.0×10^9 Pa, 0.25, 0.9, 2500 kg/m^3, and 2700 kg/m^3, respectively. For particles, we use a mixture of three types of spherical particles with diameters of 1.7, 2.0, and 2.3 mm in a quantity ratio of 1:2:1. We set the timestep Δt to 4.0×10^{-6} s with reference to the Rayleigh timestep calculated from these parameters. The above parameters, including density and particle size distribution, deviate from actual soil and granular particles. However, even with these settings, we have confirmed that DEM can reproduce F_p of actual granular materials by varying the remaining parameters [49]. Therefore, in this study, these parameters are fixed for all granular types.

In the simulations, we use four granular types (A, B, C, and D) by varying μ_{gg} and χ. Here, μ_{gg} and χ are considered to correspond effectively to particle surface friction and particle shape. Thus, various granular materials can be simulated by changing these values. In fact, we can create various sand piles by changing μ_{gg} and χ and measure ϕ from their slope angles. Sand piles are created using the following method. A saucer is placed at the bottom of a hollow cylinder (dimension: 200 mm in diameter and 200 mm in height). As in the initial packing of our previous studies [35, 49], randomly generated particles in $\mu_{gg} = 0.3$ and $\chi = 0$ are rained down to fill the cylinder. After the initial packing, μ_{gg} and χ are changed to the desired values and relaxed for 1 s. The sand pile is then created by vertically lifting the cylinder and waiting until the particles stop discharging. The value of ϕ is measured using the least-squares method to the particle positions on the surface slope. As shown in Table 1, each ϕ is set as 17.3 deg for Type A, 25.0 deg for Type B, 35.6 deg for Type C, and 38.6 deg for Type D. The simulated sand piles for each ϕ are as shown in our previous study [35].

In addition to above different ϕ, we use two different cohesive condition for each granular type. In the case of dry condition, we set $C = 0$ Pa, while in the case of cohesive condition, we set C to the values listed in Table 1. The values of C for cohesive conditions are set to satisfy $\frac{C}{\mu_{gg}} = 1000$ Pa. The reason for this definition is to ensure the same cohesive stress between particles, regardless of the granular type. Furthermore, the value of 1000 Pa for the interparticle cohesive stress is set based on previous studies investigating the cohesive stress in wet granular materials.[44, 49]. Therefore, we consider this setting to be a reasonable value that can reproduce the attraction force due to the capillary targeted on the cohesive bond force model employed in this study.

2.1.3 Simulation conditions

We perform penetration simulations by changing granular and intruder properties to investigate the effects of granular type (ϕ), cohesion (C), interface friction (friction coefficient between the intruder and particles μ_{og}), and horizontal cross-sectional geometry of intruder on F_p. Specifically, we perform penetration simulations under a total of 280 different conditions, divided into two main cases: one in which we mainly change the intruder shape and other in which we mainly change the interface friction.

First, we explain the simulation setup common to all cases. As this setup is same as our previous studies [35, 49], we explain an overview here. The simulation setup is shown in Fig.1a. The initial packing condition is adjusted to $\phi = 0.6$ using a similar method that used to create the sand pile. The dimensions of the layer are 300 mm in width and depth and 180 mm in height, respectively. Our previous study has confirmed that these dimensions are sufficiently large for the intruder size and that there is no effect on the boundaries [49]. The edge of width (x-axis) and depth (y-axis) directions are periodic boundaries. Thus, particles moving to coordinates below 0 mm or above 300 mm appear from the opposite sides. In the height (z-axis) direction, the fixed flat floor is set at the bottom of layer (z = 0 mm) to prevent particles from falling. Whereas the surface of a granular layer (z = 180 mm) is not set any boundary condition, thus, it allows particles move freely near the surface of a layer. The intruder positioned with the center of the granular surface penetrates to the layer at constant velocity $v_p = 50$ mm/s. This velocity is sufficiently smaller than the criteria of quasi-static velocity $\sqrt{4r^*g} = 200$ mm/s often used in previous studies [39–41]. As shown in Fig. 1b, penetration depth z_p is defined as the depth to the tip from the initial free surface level of granular layer. The penetration simulations continue until the intruder is completely buried in granular layer.

Next, we explain the detailed conditions for the two main cases. When mainly changing the intruder shape, we perform simulations with a total of 120 conditions, combining a fixed interface friction of 0.3, 4 granular types, 2 cohesion values, 5 intruder tip angles, and 3 intruder shapes. The three intruder shapes, cone, square pyramid (SP), and triangular

Table 1 DEM parameter list

Material type	A	B	C	D
Young's modulus E [Pa]	1.0×10^9			
Poisson ratio ν [-]	0.25			
coefficient of restitution e [-]	0.9			
particle diameter $d_1,\ d_2,\ d_3$ [mm]	1.7, 2.0, 2.3			
particle mixing ratio $d_1 : d_2 : d_3$ [-]	1 : 2 : 1			
particle density ρ_g [kg/m^3]	2500			
intruder density ρ_o [kg/m^3]	2700			
timestep Δt [s]	4.0×10^{-6}			
friction coefficient μ_{og} (intruder - particle) [-]	0.0, 0.1, 0.3, 0.5, 0.7			
friction coefficient μ_{gg} (particle - particle) [-]	0.1	0.2	0.8	1.0
shape parameter χ [-]	0.05	0.2	0.6	1.0
cohesive stress parameter C [Pa]	100	200	800	1000
angle of repose ϕ [deg]	17.3	25.0	35.6	38.6

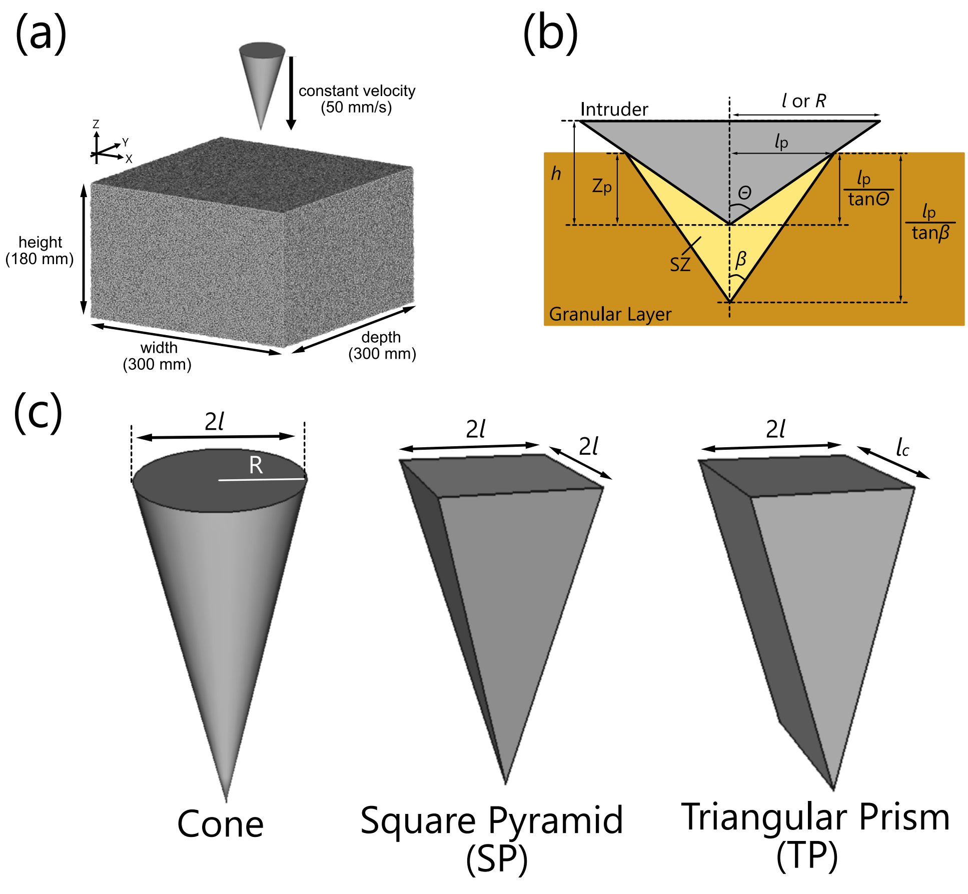

Fig. 1 **a** Schematic of simulation setup. **b** Schematic in vertical cross-section view of the intruder penetrating to granular layer. A conical stagnant zone (SZ) with a tip angle β is formed in front of the intruder. Using l_p, the penetration heights of the intruder and the stagnant zone are calculated as $\frac{l_p}{\tan\Theta}$ and $\frac{l_p}{\tan\beta}$, respectively. **c** Intruder shapes used in this study. From left to right: cone, square pyramid (SP), triangular prism (TP)

prism (TP), are shown in Fig. 1c. The reason for selecting SP and TP is that their tip angle of vertical cross sections can be defined by Θ in the same way as a cone, allowing us to examine the effect of horizontal cross-sectional geometry on F_p. In addition, since these shapes resemble claws of the construction machinery and animals, verifying them will be useful in expanding the applications for the extended MALT. The dimensional information regarding the half base length l (or radius of cone R), height h, and side length l_c (TP only) for each shape is shown in Table 2. As mentioned in our previous study [35], the value of R is set based on the cone specifications of the Japanese Geotechnical Society Standards 1431. In SP and TP, we set l so that the base area is similar to that of the cone, and l_c so that the base shape of SP is a regular quadrilateral. When mainly changing the interface friction, we perform simulations for a total of 160

Table 2 Details of the intruder shapes used in this study

Shape	Length	Tip angle 15 deg	30 deg	45 deg	60 deg	75 deg
Cone	$l\ (= R)$ [mm]	28.6	28.6	42.9	42.9	42.9
	h [mm]	106.7	49.5	42.9	24.8	11.5
SP	l [mm]	25	25	37.5	37.5	37.5
	h [mm]	93.3	43.3	37.5	21.7	10.0
TP	l [mm]	25	25	37.5	37.5	37.5
	l_c [mm]	50	50	75	75	75
	h [mm]	93.3	43.3	37.5	21.7	10.0

conditions, combining a fixed intruder shape of a cone, 4 granular types, 2 cohesion values, 5 intruder tip angles, and 4 interface frictions excluding 0.3, as shown in Table 1.

2.1.4 Simulation results

The simulation results for granular type C are shown in the cases where the intruder shape is mainly changed (Fig. 2) and where the interface friction is mainly changed (Fig. 3). As we have reported [49], Figs. 2 and 3 indicate that the magnitude of F_p and the relationship between F_p and z_p change depending on Θ and C. Furthermore, these figures indicate that the relationship between F_p and z_p also changes depending on the intruder shape.

2.2 Theoretical study

2.2.1 Theoretical model

This section provides an overview of the extended MALT model. For derivation and other details, see our previous study [49]. According to the extended MALT model, F_p against an cohesive granular layer is expressed by the following equation:

$$F_p(z_p) = f(\Theta) K_\phi \rho_g \psi g V_p(z_p) + K_c C' S_p(z_p), \tag{4}$$

where C' is the bulk cohesive stress of a granular layer in the model. Here, C' is set to C for each granular type based on our previous study [49]. V_p and S_p represent the volume and the horizontal cross-sectional area of a penetrated intruder, respectively. The specific forms of V_p and S_p for each intruder shape are geometrically expressed as follows:

$$V_p(z_p) = \begin{cases} \frac{1}{3}\pi z_p^3 \tan^2\Theta, & \text{(Cone)}, \\ \frac{4}{3} z_p^3 \tan^2\Theta, & \text{(SP)}, \\ l_c z_p^2 \tan\Theta, & \text{(TP)}. \end{cases} \tag{5}$$

$$S_p(z_p) = \begin{cases} \pi z_p^2 \tan^2\Theta, & \text{(Cone)}, \\ 4 z_p^2 \tan^2\Theta, & \text{(SP)}, \\ 2 l_c z_p \tan\Theta, & \text{(TP)}. \end{cases} \tag{6}$$

In Eqs. (5) and (6), V_p is proportional to the cube of z_p for cone and SP, and to the square of z_p for TP. Similarly, S_p is proportional to the square of z_p for cone and SP, and linearly proportional to z_p for TP. Coefficients K_ϕ and K_c depend only on ϕ, and these are described by the following equations [31, 49]:

$$\begin{aligned} K_\phi &\equiv \left(2\frac{1+\sin\phi}{1-\sin\phi} e^{\pi\tan\phi} \int_0^1 \eta A(\eta,\phi) d\eta\right), \\ K_c &\equiv \left(2\frac{1+\sin\phi}{1-\sin\phi} e^{\pi\tan\phi} \int_0^1 \eta A(\eta,\phi) d\eta - 2\int_0^1 \eta d\eta\right)\cot\phi \\ &= \left(K_\phi - 2\int_0^1 \eta d\eta\right)\cot\phi, \end{aligned} \tag{7}$$

where η and $A(\eta, \phi)$ are dimensionless parameters in the model. $A(\eta, \phi)$ and its associated quantities are computed as follows [31, 49]:

$$\begin{cases} A(\eta,\phi) = \left(\dfrac{r_1^{1+\tan^2\beta}}{r_2^{\tan^2\beta} r_3}\right)^{\sin\phi} e^{\sin\phi\tan\beta Z(\eta,\phi)}, \\ r_1 = R_p\left(1 + \frac{2(1-\eta)}{\tan\beta} e^{\frac{\pi}{2}\tan\phi}\right), \\ r_2 = R_p\left(1 + \frac{1-\eta}{\tan\beta} e^{\frac{\pi}{2}\tan\phi}\right), \\ r_3 = R_p\eta, \\ Z(\eta,\phi) = \int_{r_3}^{r_2} \frac{dz}{r} = \int_0^{\frac{\pi}{2}} \frac{(\eta-1)e^{\lambda\tan\varphi}\cos(\lambda+\beta)}{\cos\varphi[\sin\beta + (1-\eta)e^{\lambda\tan\varphi}\sin(\lambda-\beta)]} d\lambda, \end{cases} \tag{8}$$

where λ is also a dimensionless parameter in the analysis, and β represents the tip angle of the stagnant zone formed in front of an intruder [5, 31, 32]. This angle is defined as $\beta = \frac{\pi}{4} - \frac{\phi}{2}$. From the above, the variations of K_ϕ and K_c with ϕ are shown in Fig. 4a. The values of K_ϕ and K_c for each granular type are shown in Table. 3. ("General Failure" corresponds to this result.) The correction factor $f(\Theta)$ in Eq. (4) is expressed as follows:

$$f(\Theta) = \begin{cases} \frac{\tan\Theta}{\tan\beta} & \text{if } \Theta > \beta, \\ 1 & \text{if } \Theta \le \beta, \end{cases} \tag{9}$$

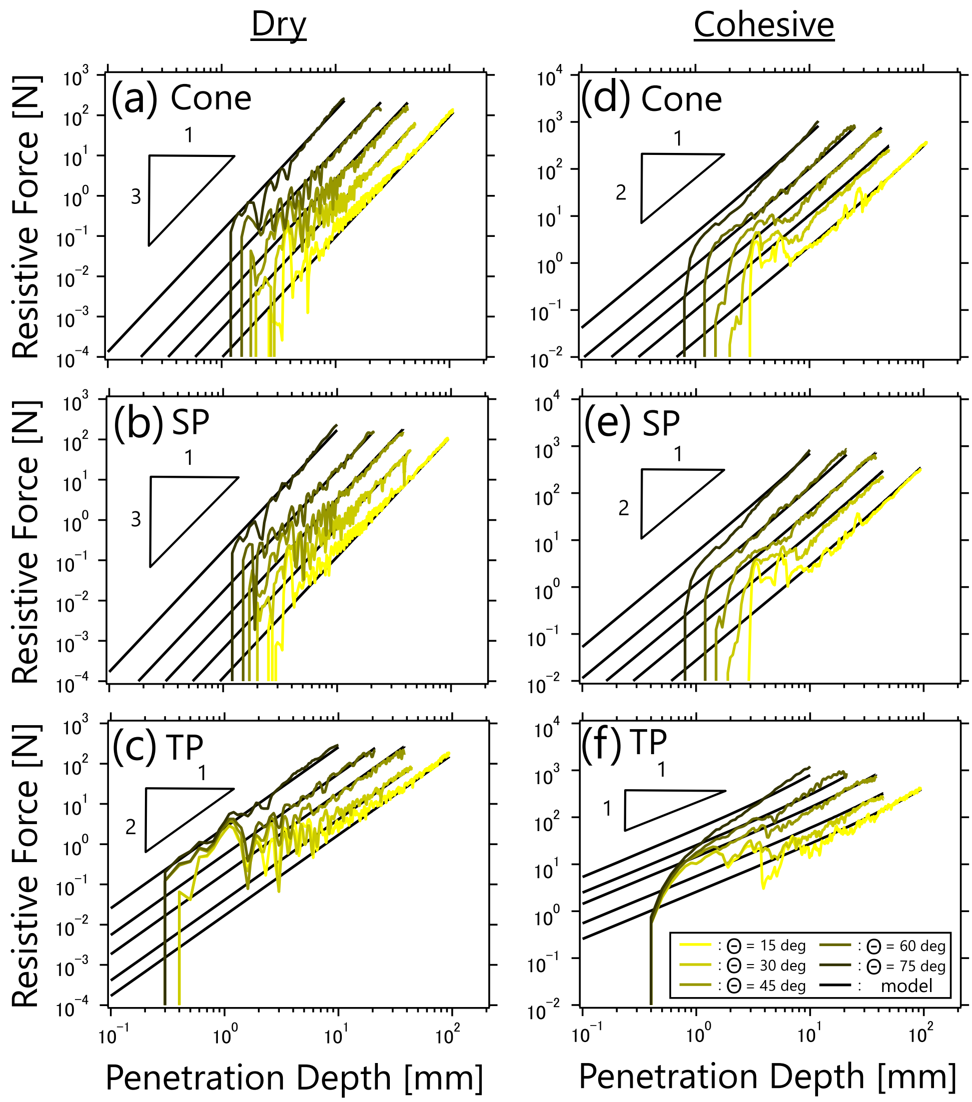

Fig. 2 Relationship between F_p and z_p for granular type C in dry and cohesive conditions. **a**, **d** Cone, **b**, **e** square pyramid (SP), and **c**, **f** triangular prism (TP). The horizontal axis is z_p, and the vertical axis is F_p in log–log scale. Colored lines indicate the simulation results with different Θ. The black solid lines are F_p computed by the modified model

Table 3 K_ϕ and K_c for each type

Material type	A	B	C	D
K_ϕ (General Failure)	7.3	20.0	103.7	177.8
K_c (General Failure)	20.1	40.8	143.4	221.5
K_ϕ (Punching)	4.9	10.7	36.0	53.1
K_c (Punching)	12.6	20.8	48.8	65.3

This correction factor models the tip effect by considering the stagnant zone as an effective tip shape [35, 49].

The terms on the right-hand side of Eq. (4), except for $f(\Theta)$, are derived using a slip-line field analysis assuming cohesive granular materials. In this model, a granular layer is treated as a continuous body, and the equilibrium of stresses is considered. Based on the Mohr–Coulomb yield criterion, the stress along the slip line during intruder penetration can be obtained from characteristic curves [37, 38, 43]. As a result, these terms are derived by calculating the sum of the resistive stresses on the stagnant zone and the slip lines. The validity of these terms has been empirically verified through experiments and simulations [31, 32, 35, 41, 49]. The physical interpretation of each term on the right-hand side of Eq. (4) is as follows: The first term represents hydrostatic-like forces arising from the friction between particles confined by gravity, while the second term represents forces originating from the cohesive stress associated with displacements in the shear zone. Therefore, these terms are proportional to the penetrated intruder volume and horizontal cross-sectional area, respectively.

2.2.2 Model assessment

We compute F_p for each simulation condition using Eq. (4). The linear regression is performed on the computed and simulated F_p to obtain the slope k and the coefficient

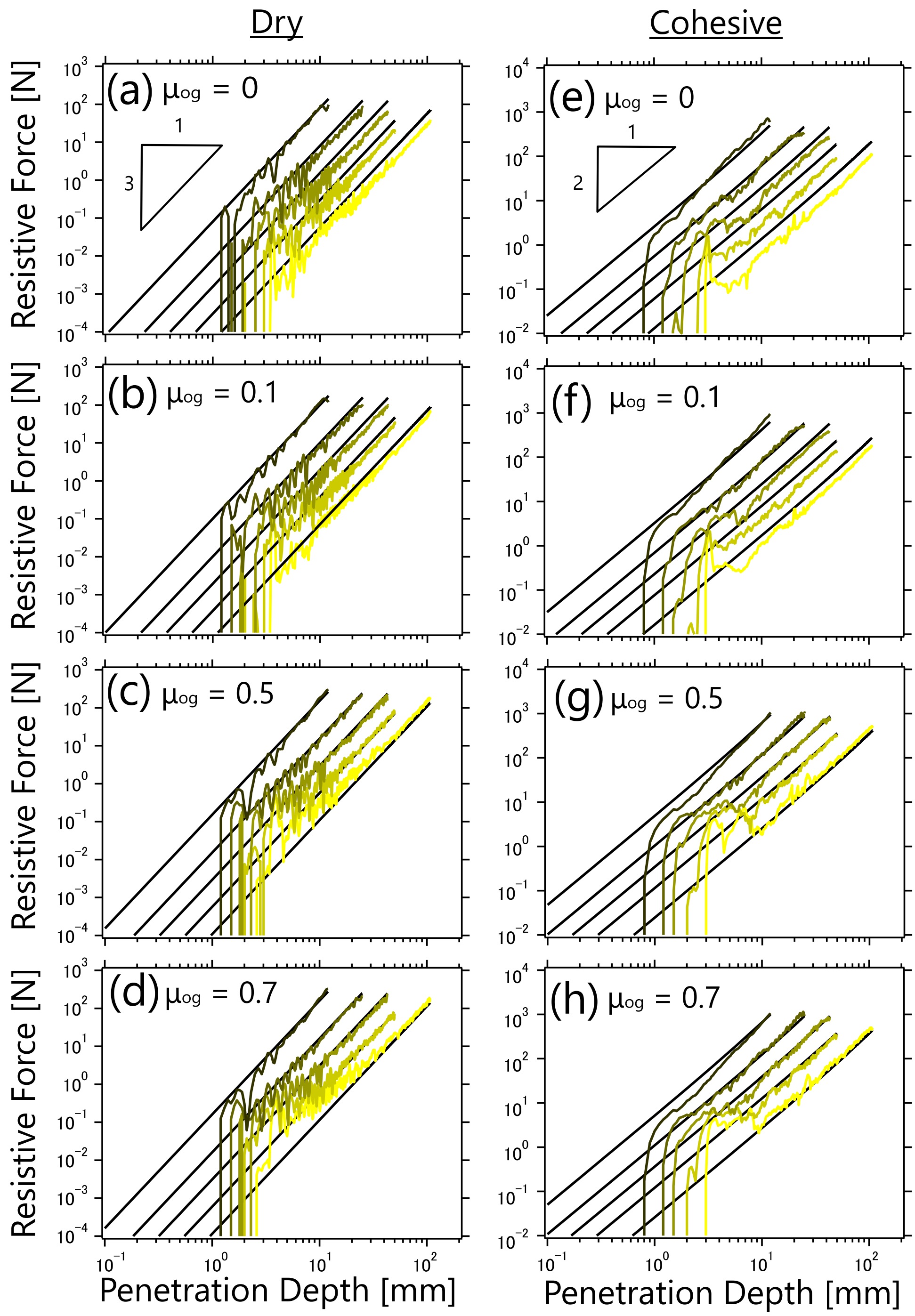

Fig. 3 Relationship between F_p and z_p for granular type C in dry and cohesive conditions. **a**, **e** $\mu_{og} = 0$, **b**, **f** $\mu_{og} = 0.1$, **c**, **g** $\mu_{og} = 0.5$, and **d**, **h** $\mu_{og} = 0.7$. The horizontal axis is z_p, and the vertical axis is F_p in log–log scale. Colored lines indicate the simulation results with different Θ. The black solid lines are F_p computed by the modified model

of determination R^2. The values of k are calculated by the following equation:

$$k = \frac{F_{p,model}}{F_{p,DEM}}, \tag{10}$$

where $F_{p,model}$ is the computed value by the extended MALT, and $F_{p,DEM}$ is the value obtained by the simulation. The values of k and R^2 for each simulation condition are shown in Table 4. In addition, as an indicator of the model's predictive accuracy, calculating the mean value of $|k - 1|$, we obtain $|k - 1| = 0.486 \pm 0.521$ from Table 4.

From the data in Table 4, we evaluate the prediction accuracy of the model in detail. Regarding R^2 in Table 4, the values are high regardless of the simulation conditions. However, it is difficult to examine the factors affecting F_p since the extended MALT consists of two terms with different factors. To simplify the identification of the factors affecting F_p, we introduce the characteristic penetration depth, z_p^*, as

Table 4 The values of k and R^2 obtained by linear regression of the current model and simulation results

Condition	$\frac{C}{\mu_{gg}}$ [kPa]	k for Type A	k for Type B	k for Type C	k for Type D
Cone	0	1.91 (R^2: 0.99)	2.90 (R^2: 0.99)	3.35 (R^2: 0.98)	2.77 (R^2: 0.94)
(μ_{og}=0.0)	1	0.88 (R^2: 0.99)	1.41 (R^2: 0.99)	2.93 (R^2: 0.98)	2.56 (R^2: 0.98)
Cone	0	1.54 (R^2: 0.99)	2.18 (R^2: 1.00)	2.17 (R^2: 0.99)	1.61 (R^2: 0.97)
(μ_{og}=0.1)	1	0.71 (R^2: 0.99)	1.08 (R^2: 1.00)	1.96 (R^2: 0.99)	1.66 (R^2: 0.98)
Cone	0	1.37 (R^2: 0.99)	1.58 (R^2: 1.00)	1.21 (R^2: 0.99)	0.79 (R^2: 0.97)
(μ_{og}=0.3)	1	0.62 (R^2: 0.99)	0.82 (R^2: 1.00)	1.19 (R^2: 0.99)	0.95 (R^2: 0.99)
SP	0	1.32 (R^2: 0.99)	1.48 (R^2: 0.99)	1.14 (R^2: 0.98)	0.74 (R^2: 0.98)
(μ_{og}=0.3)	1	0.60 (R^2: 0.99)	0.83 (R^2: 0.99)	1.20 (R^2: 0.99)	0.99 (R^2: 0.99)
TP	0	1.32 (R^2: 0.99)	1.47 (R^2: 0.99)	1.16 (R^2: 0.98)	0.72 (R^2: 0.92)
(μ_{og}=0.3)	1	0.59 (R^2: 0.99)	0.77 (R^2: 0.99)	1.10 (R^2: 0.98)	0.87 (R^2: 0.98)
Cone	0	1.37 (R^2: 0.99)	1.54 (R^2: 0.99)	0.99 (R^2: 0.99)	0.58 (R^2: 0.95)
(μ_{og}=0.5)	1	0.62 (R^2: 0.99)	0.80 (R^2: 1.00)	0.97 (R^2: 0.99)	0.72 (R^2: 0.99)
Cone	0	1.37 (R^2: 0.99)	1.53 (R^2: 1.00)	1.00 (R^2: 0.99)	0.56 (R^2: 0.95)
(μ_{og}=0.7)	1	0.62 (R^2: 0.99)	0.79 (R^2: 1.00)	0.94 (R^2: 0.99)	0.67 (R^2: 0.99)

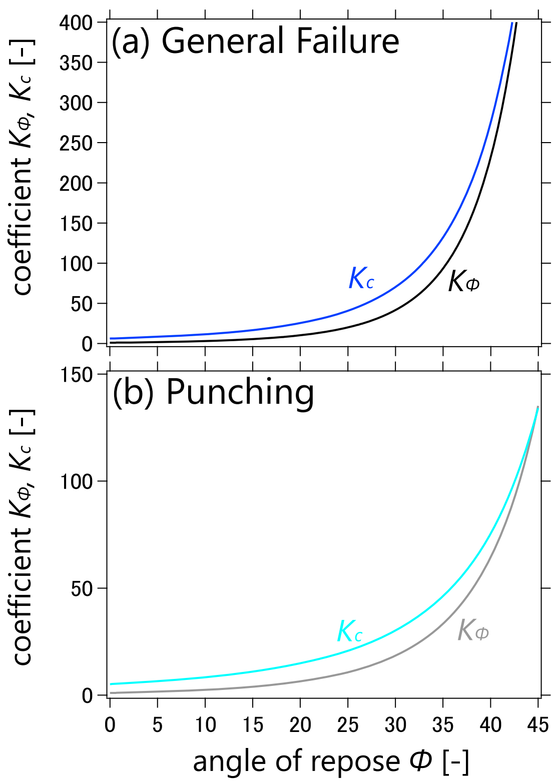

Fig. 4 Variations of K_ϕ and K_c computed by Eq. (7) with respect to ϕ for **a** general failure and **b** punching. The values of K_ϕ for each mode are shown as the black line in (**a**) and the gray line in (**b**), respectively. That of K_c for each mode are shown as the blue line in (**a**) and the light blue line in (**b**), respectively

follows:

$$z_p^* = \begin{cases} \frac{3k_c C'}{f(\Theta)k_\phi \rho_g \psi g}, & \text{(Cone, SP)}, \\ \frac{2k_c C'}{f(\Theta)k_\phi \rho_g \psi g}, & \text{(TP)}. \end{cases} \tag{11}$$

Here, z_p^* represents the penetration depth at which these two terms in the right-hand side of extended MALT are balanced. In other words, below z_p^*, the cohesion-derived second term is dominant. For example, $z_p^* = 0$ mm in dry cases indicates that F_p depends solely on the friction-derived first term ($F_p \propto V_p$). In contrast, in cohesive cases for type C, $z_p^* \sim 150$ mm, which is higher than h for each intruder shape, suggests that F_p mainly depends on the cohesion-derived second term ($F_p \propto S_p$). In fact, simulation results in Figs. 2 and 3 show a similar trend to these indications. Since a similar trend is observed for the other types, it is reasonable to conclude that F_p is subjected to the friction-derived term in dry cases and to the cohesion-derived term in cohesive cases under our simulation conditions.

Regarding the values of k in Table 4, the values vary depending on the granular type, cohesion, and interface friction, while the intruder shape has minimal influence. First, we focus on the effect of granular type. In dry cases, types A and B tend to exhibit larger k values compared to types C and D. In cohesive cases, types A and B tend to show smaller k values compared to types C and D. This tendency suggests that the prediction accuracy of the extended MALT depends on the granular type. With respect to cohesion, even for the same granular type, the k value can vary significantly depending on the presence of cohesion. This is probably because the principal origin of F_p changes due to cohesion. Regarding the interface friction, it is evident that k increases as μ_{og} decreases, regardless of the granular type. This result indicates that the simulated F_p decreases with μ_{og} since the current extended MALT computes F_p independent of μ_{og}. Therefore, it is clear that the current model cannot adequately account for the effects of granular type, cohesion, and interface friction, indicating the necessary of modification.

3 Model modification

3.1 Analysis of failure modes

In geotechnical engineering, Vesić [28] has reported that the failure mechanism during penetration can be classified into three modes—general failure, local failure, and punching—each of which affects resulting F_p. As explained in 2.2.1, the MALT assumes that the failure is characterized by slip lines propagating to the ground surface and the formation of a distinct shear band. It means that the MALT only considers the general failure in granular layer when an intruder penetrates. However, the failure modes generally relate to material properties such as ϕ and ψ. Therefore, local failure and punching might be dominant depending on the granular type.

To identify the failure modes for each granular type, we analyze the distribution of shear strain rate $\dot{\gamma}$ in granular layer [4–6]. In this study, $\dot{\gamma}$ is defined as the following equation:

$$\dot{\gamma} = \sqrt{\left(\frac{\dot{e}_{xx} - \dot{e}_{zz}}{2}\right)^2 + \dot{e}_{xz}^2}, \tag{12}$$

where the normal strain rates $\dot{e}_{xx}$ and $\dot{e}_{zz}$ and the shear strain rate $\dot{e}_{xz}$ are, respectively, defined as follows:

$$\begin{cases} \dot{e}_{xx} = \frac{\partial u_x}{\partial x} \\ \dot{e}_{zz} = \frac{\partial u_z}{\partial z} \\ \dot{e}_{xz} = \frac{1}{2}\left(\frac{\partial u_x}{\partial z} + \frac{\partial u_z}{\partial x}\right). \end{cases} \tag{13}$$

In the actual analysis, we calculate $\dot{\gamma}$ in each 2 mm grid using the velocity of particles existing in the central cross-sectional area (xz plane) of the granular layer. Figure 5 illustrates the $\dot{\gamma}$ distributions for TP with $\Theta = 45$ deg in each granular type at the final penetration state.

Figure 5 indicates that $\dot{\gamma}$ distributions vary depending on the granular types. Specifically, for type A and B, particles with high $\dot{\gamma}$ are distributed only around the penetrating intruder. In contrast, for type C and D, the regions of high $\dot{\gamma}$ extend not only around the intruder but also toward the surface of the granular layer, forming a band. Comparing these results with the failure modes classified by Vesić [28], type A and B correspond to the punching, while type C and D correspond to the general failure.

3.2 Parameter determination

3.2.1 Coefficients K_ϕ and K_c

The analysis results of the $\dot{\gamma}$ distributions suggest that the failure mechanism of granular types A and B is punching. Here, we consider K_ϕ and K_c assuming punching failure and examine the correspondence with the simulation results. When the punching mode is assumed, the values of $A(\eta, \phi)$ and $Z(\eta, \phi)$ in Eq. (8), respectively, equal 1 and 0 due to $r_1 = r_2 = r_3$. As a result, K_ϕ and K_c for the punching mode are as follows:

$$\begin{aligned} K_\phi &= \left(2\frac{1+\sin\phi}{1-\sin\phi}e^{\pi\tan\phi}\int_0^1 \eta d\eta\right), \\ K_c &= \left(2\frac{1+\sin\phi}{1-\sin\phi}e^{\pi\tan\phi}\int_0^1 \eta d\eta - 2\int_0^1 \eta d\eta\right)\cot\phi \\ &= \left(K_\phi - 2\int_0^1 \eta d\eta\right)\cot\phi. \end{aligned} \tag{14}$$

The variations of K_ϕ and K_c with ϕ assuming punching mode are shown in Fig. 4b. Moreover, these specific K_ϕ and K_c values for each granular type under punching mode are summarized in Table 3.

Next, we evaluate the values of K_ϕ and K_c used in the model by analyzing the simulation results. Focusing on the dry cases, we estimate K_ϕ from the simulated F_p for each granular type. As mentioned in Sec. 2.2.2, it is clear that F_p is proportional to V_p in the dry cases. From a linear relationship between F_p and $f(\Theta)\rho_g\psi g V_p$, we calculate the slope using the least-squares method. This slope is regarded as the estimated K_ϕ derived from the simulation results. Figure 6 presents the estimated values of K_ϕ for each granular type, intruder shape, and μ_{og}. Here, we focus on the case where μ_{og} is sufficiently large, and K_ϕ reaches the saturated value, even though Fig. 6 shows that K_ϕ varies with μ_{og}. Comparing the estimated values of K_ϕ with the theoretically calculated values, Fig. 6 reveals that the estimated K_ϕ for types C and D are close to the theoretical values for the general failure mode. Conversely, the estimated values of K_ϕ for types A and B appear to be closer to the theoretical values assuming the punching mode. Moreover, Fig. 5 shows that the failure mode is independent of the cohesion of the granular layer. Based on these findings, in this study, we use the values of K_ϕ and K_c for punching with types A and B, while using the values for general failure with types C and D.

3.2.2 Model cohesive stress C′

In addition to K_ϕ and K_c, we need to determine C' in the model. In our previous study [49], we have assumed $C' = C$. However, it remains unclear whether this relation-

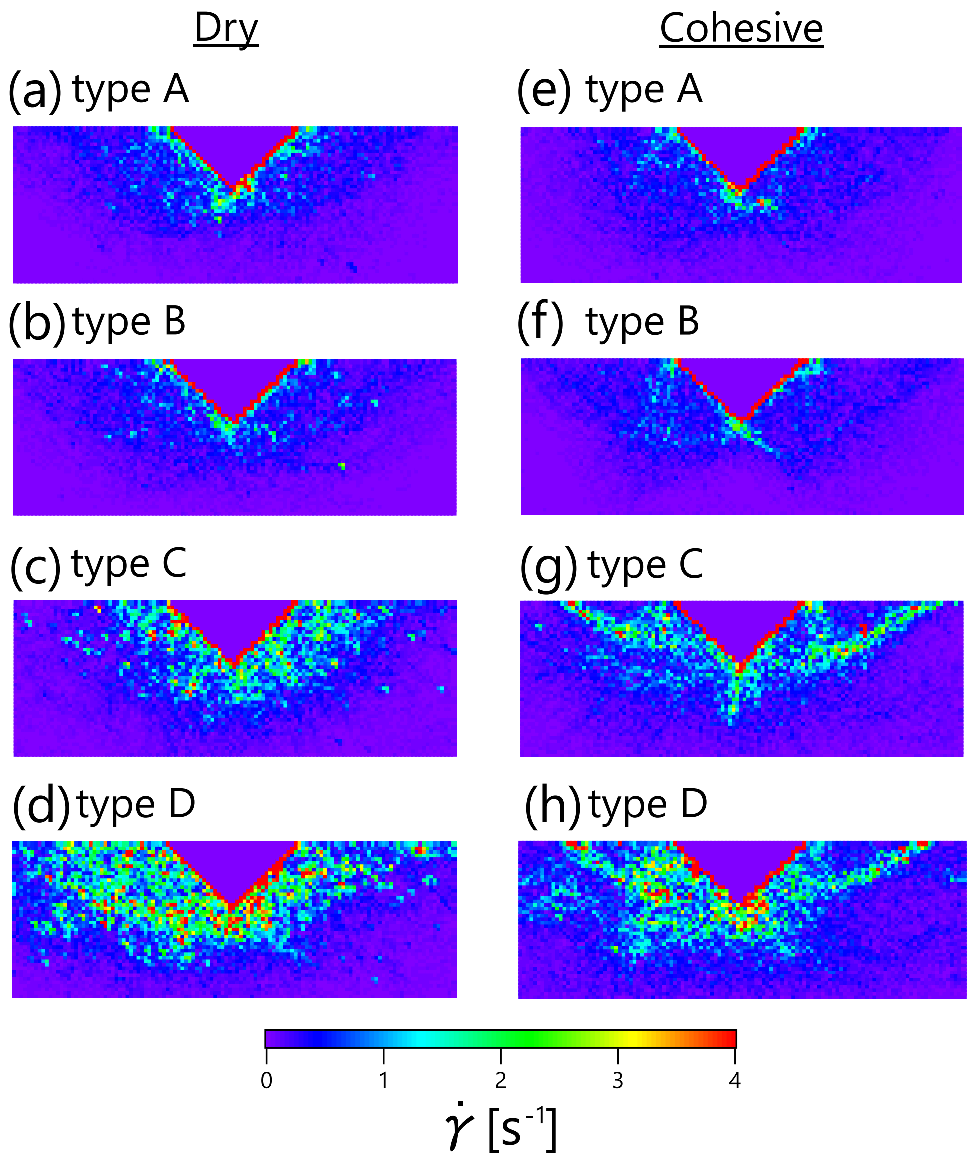

Fig. 5 The $\dot{\gamma}$ distributions in vertical cross-section view on TP of $\Theta = 45$ deg for **a**–**d** dry cases, **e**–**h** cohesive cases. As the color bar indicates, the higher the value of $\dot{\gamma}$, the warmer the color

ship holds across different granular types. Therefore, based on the simulation results, we clarify the relationship C' and DEM parameters.

In cohesion cases, as mentioned in Sec. 2.2.2, F_p is proportional to S_p. Assuming a linear relationship between F_p and $K_c S_p$, we calculate the slope using the least-squares method. This slope is regarded as the estimated C' derived from the simulation results. Figure 7 shows the estimated values of C' for each granular type, intruder shape, and μ_{og}.

From Fig. 7, we examine the relationship between C' and the DEM parameters in the simulation. Here, we focus on the case where C' reaches saturation, as observed for K_p and K_c. First, we assume $C' = C$, as used in our previous study [49]. Comparing the estimated values of C' with C for each granular type, as shown in Table 1, we find that the estimated C' values are close to C for types C and D. In contrast, for types A and B, there is a significant discrepancy between the estimated C' and C. In fact, the estimated values of C' are approximately four times larger than C for type A. Next, we assume $C' = \frac{C}{\mu_{gg}} = 1000$ Pa. The definition $\frac{C}{\mu_{gg}}$ represents the relative cohesive stress compared to friction between particles set in the simulation. Under this assumption, for types A, B, and C, $\frac{C}{\mu_{gg}}$ is larger than the estimated C' values. We further consider the assumption $C' = \psi \frac{C}{\mu_{gg}} = 600$ Pa. This definition represents the effective bulk cohesive stress of the simulated granular layer, taking into account that cohesive stresses do not act in the voids. Under this assumption, the estimated values of C' are in good agreement with $\psi \frac{C}{\mu_{gg}}$ for type B, whereas the estimated C' values for type A are smaller than $\psi \frac{C}{\mu_{gg}}$. However, this assumption can explain the estimated C' values for type A within a factor of two through the DEM parameters. Taken together with the results

Fig. 6 Variation of the estimated K_ϕ with respect to μ_{og} for **a** type A, **b** type B, **c** type C, and **b** type D. The vertical axis is the estimated K_ϕ and the horizontal axis is μ_{og} in log-linear scale. Markers indicate the mean value of the estimated K_ϕ with Θ, and error bars indicate its standard deviation. Marker geometries represent differences in intruder shape. (◯ : Cone, □ : SP, and △ : TP). The solid lines are the theoretically calculated values of K_ϕ for general failure. The dashed lines are the theoretically calculated values of K_ϕ for punching

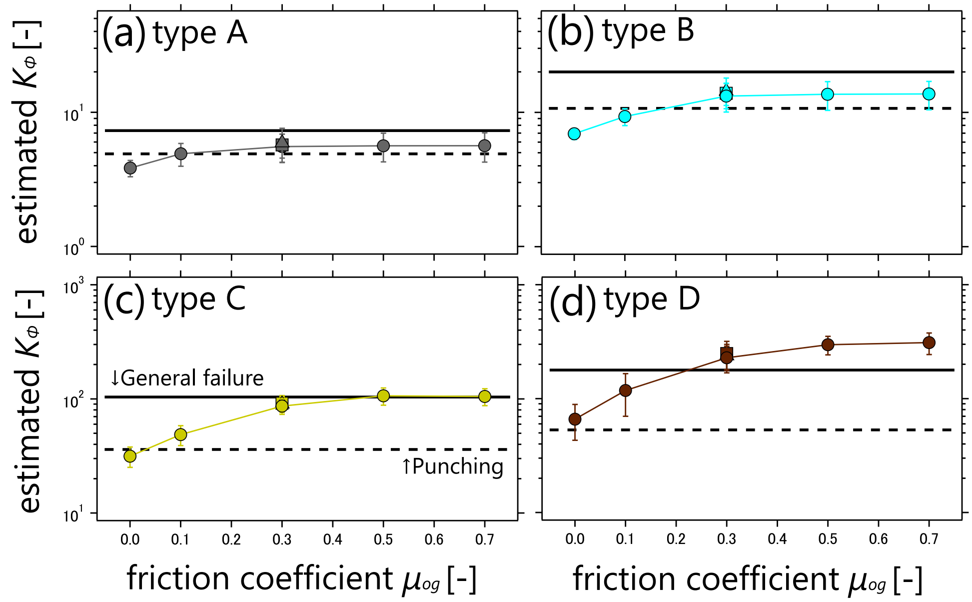

Fig. 7 Variation of the estimated C' with respect to μ_{og} for **a** type A, **b** type B, **c** type C, and **b** type D. The vertical axis is the estimated C', and the horizontal axis is μ_{og} in log-linear scale. Markers indicate the mean value of the estimated C' with Θ, and error bars indicate its standard deviation. Marker geometries represent differences in intruder shape. (◯ : Cone, □ : SP, and △ : TP). The dotted lines are the values of $C' = C$ for each granular type. The dashed lines are $C' = \frac{C}{\mu_{gg}} = 1000$ Pa. The solid lines are $C' = \psi \frac{C}{\mu_{gg}} = 600$ Pa

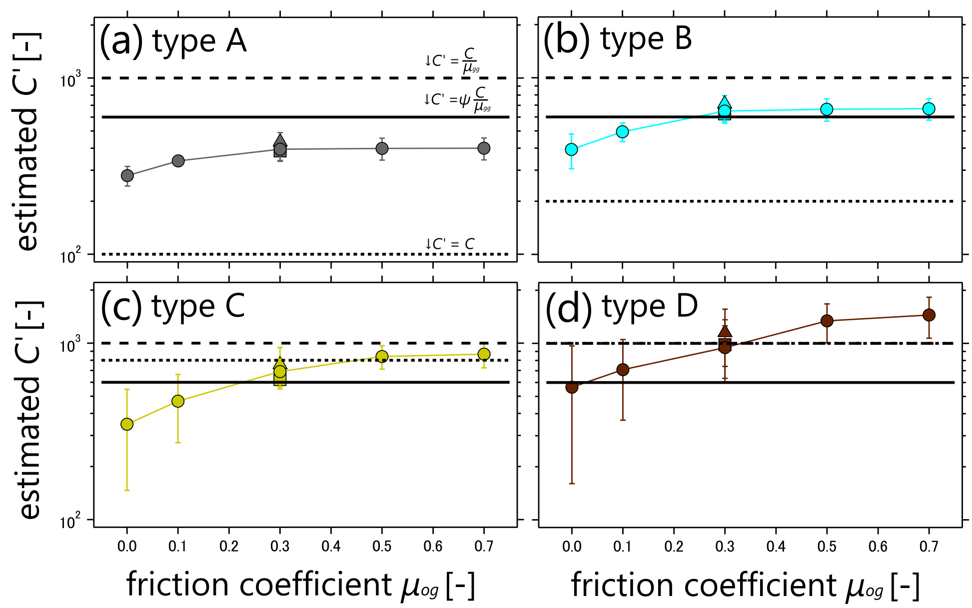

in Section 3.2.1, these differences in cohesive stress may correspond to the failure modes of the granular layer. Therefore, we adopt $C' = \psi \frac{C}{\mu_{gg}}$ for punching (types A and B), and $C' = C$ for general failure (types C and D) as the bulk cohesive stress in the model expressed by the DEM parameters.

3.3 Incorporating the effect of μ_{og} into the model

Assuming that C' is constant for each granular type, Figs. 6 and 7 show that K_ϕ and K_c vary with μ_{og} and saturate to a certain value. Here, we incorporate the effect of μ_{og} into K_ϕ and K_c. In previous studies, Xi et al. [52] have argued that the model coefficient K relating to F_p varies with the ratio of μ_{og} to $\tan\phi$. Specifically, the effect of μ_{og} on K is expressed by the following equation:

$$K^{\mu_{og}} = \left(n + \frac{1-n^2}{2}\right)K, \tag{15}$$

where $K^{\mu_{og}}$ is the value of K at μ_{og}; n is the ratio of μ_{og} to $\tan\phi$ (i.e., $n = \frac{\mu_{og}}{\tan\phi}$). This equation implies that $K^{\mu_{og}}$ rapidly saturates to K with $\mu_{og} \neq 0$, though $K^{\mu_{og}}$ decreases to half the value of K with $\mu_{og} = 0$. Xi et al. [52] have applied Eq. (15) to the coefficient derived from different modeling from this study. However, it is similar in terms of the influence of μ_{og} on the coefficients related to F_p. Moreover, as shown in Fig. 8, the particle velocity fields support that the shape of the stagnant zone changes with μ_{og}. Thus, it would be

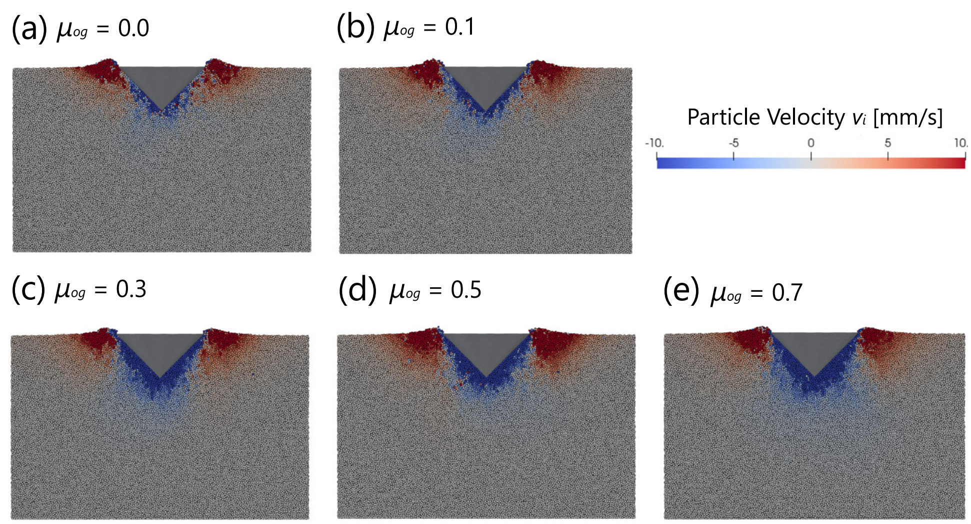

Fig. 8 Particle velocity fields in vertical cross-section view on cone of $\Theta = 45$ deg for type B with **a** $\mu_{og} = 0.0$, **b** $\mu_{og} = 0.1$, **c** $\mu_{og} = 0.3$, **d** $\mu_{og} = 0.5$, and **e** $\mu_{og} = 0.7$. As represented by the color bar, red and blue indicate positive and negative particle velocities in z-direction, respectively

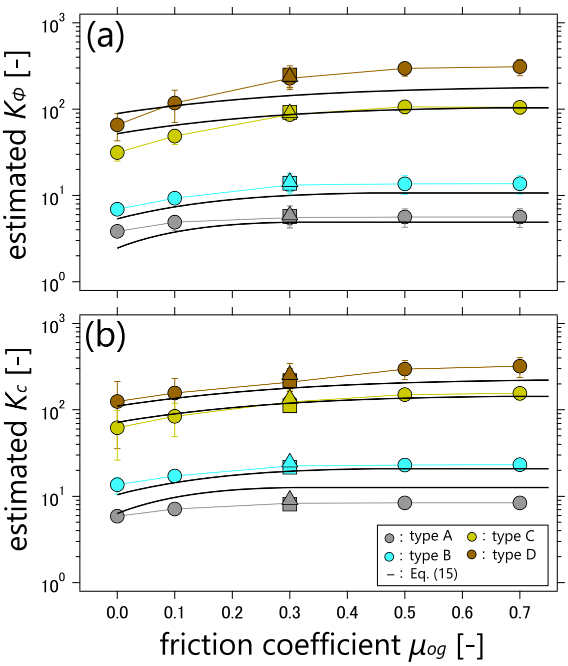

Fig. 9 Variation of the estimated **a** K_ϕ and **b** K_c with respect to μ_{og}. The vertical axis is the estimated coefficients and the horizontal axis is μ_{og} in log-linear scale. The colored markers and lines represent the differences in granular type. Markers indicate the mean value of the estimated C' with Θ, and error bars indicate its standard deviation. Marker geometries represent differences in intruder shape. (◯ : Cone, □ : SP, and △ : TP). The black solid lines are the values of K_ϕ and K_c calculated using Table 3 and Eq. (15)

no problem to apply Eq. (15) to K_ϕ and K_c. Figure 9 shows comparisons between calculation results of $K_\phi^{\mu_{og}}$ and $K_c^{\mu_{og}}$ with μ_{og} with the estimated values of K_ϕ and K_c from simulation results. When estimating K_c, we use the definition of C' by the DEM parameters determined in Section 3.2.2. The calculated values of $K_\phi^{\mu_{og}}$ and $K_c^{\mu_{og}}$ are in good agreement with the estimated K_ϕ and K_c for various granular types in all ranges of μ_{og}. It is clear that the μ_{og} dependence of F_p can be quantitatively taken into account by Eq. (15).

3.4 Evaluation of the modified model

Based on the values of K_ϕ, K_c and C' for each granular type and interface friction, we compute F_p from Eq. 4. To evaluate the influence of the model modification, we obtain k and R^2 through the linear regression on $F_{p,model}$ and $F_{p,DEM}$. The values of k and R^2 for each simulation condition are shown in Table 5. The mean value of $|k-1|$ is calculated as $|k-1| = 0.208 \pm 0.155$ from Table 5.

Next, we perform the analysis of variance (ANOVA) on $|k-1|$ to evaluate the significance of the granular and intruder properties. The calculated factors in ANOVA are granular type (4 levels), intruder shape (3 levels), cohesion (2 levels), and interface friction (5 levels). In addition to main effects of these factors, we include the cross-term between granular type and interface friction to ANOVA. The analysis results indicate $R^2 = 0.708$ and p value $= 0.000423$. This means that the overall model explains approximately 70.8% of the variance in $|k-1|$, and the model has statistically significant difference.

The effects of individual factors are shown in Table 6. From Table 6, the degree of influence of the factor on the total variance, η_p^2, indicates that the interaction between granular type and interface friction has the largest impact on prediction accuracy. In addition, granular type and interface friction have a large impact on the prediction accuracy. On the other hand, intruder shape and cohesion have a small impact on the prediction accuracy from these small η_p^2 values and large p value. For example, comparing the shape effects under the same simulation conditions, as shown in Table 5, the mean values of $|k-1|$ are computed as 0.165 ± 0.151 for cone, 0.182 ± 0.157 for SP, and 0.199 ± 0.125 for TP. This fact

Table 5 The values of k and R^2 obtained by linear regression of the modified model and simulation results

Condition	$\frac{C}{\mu_{gg}}$ [kPa]	k for Type A	k for Type B	k for Type C	k for Type D
Cone	0	0.66 (R^2: 0.99)	0.78 (R^2: 0.99)	1.67 (R^2: 0.98)	1.38 (R^2: 0.94)
(μ_{og}=0.0)	1	0.98 (R^2: 0.99)	0.78 (R^2: 0.99)	1.46 (R^2: 0.99)	1.28 (R^2: 0.98)
Cone	0	0.80 (R^2: 0.99)	0.81 (R^2: 1.00)	1.37 (R^2: 0.99)	1.00 (R^2: 0.97)
(μ_{og}=0.1)	1	1.23 (R^2: 0.99)	0.84 (R^2: 1.00)	1.24 (R^2: 0.99)	1.03 (R^2: 0.99)
Cone	0	0.93 (R^2: 0.99)	0.85 (R^2: 1.00)	1.01 (R^2: 0.99)	0.64 (R^2: 0.97)
(μ_{og}=0.3)	1	1.40 (R^2: 0.99)	0.91 (R^2: 1.00)	0.99 (R^2: 0.99)	0.77 (R^2: 0.99)
SP	0	0.89 (R^2: 0.99)	0.79 (R^2: 0.99)	0.95 (R^2: 0.98)	0.60 (R^2: 0.98)
(μ_{og}=0.3)	1	1.42 (R^2: 0.99)	0.93 (R^2: 0.99)	1.00 (R^2: 0.99)	0.80 (R^2: 0.99)
TP	0	0.89 (R^2: 0.99)	0.79 (R^2: 0.99)	0.96 (R^2: 0.98)	0.58 (R^2: 0.92)
(μ_{og}=0.3)	1	1.25 (R^2: 0.99)	0.82 (R^2: 0.99)	0.92 (R^2: 0.99)	0.70 (R^2: 0.98)
Cone	0	0.92 (R^2: 0.99)	0.82 (R^2: 0.99)	0.95 (R^2: 0.99)	0.54 (R^2: 0.95)
(μ_{og}=0.5)	1	1.39 (R^2: 0.99)	0.89 (R^2: 1.00)	0.92 (R^2: 0.99)	0.67 (R^2: 0.99)
Cone	0	0.92 (R^2: 0.99)	0.82 (R^2: 1.00)	1.00 (R^2: 0.99)	0.56 (R^2: 0.95)
(μ_{og}=0.7)	1	1.39 (R^2: 0.99)	0.88 (R^2: 1.00)	0.94 (R^2: 0.99)	0.67 (R^2: 0.99)

supports that the influence of intruder shape on prediction accuracy is limited. Based on the above results, we conclude that the prediction accuracy of the modified model is primarily determined by the granular type, interface friction, and their cross-term.

4 Discussion

4.1 Intruder shape

Figures 2 and 3 demonstrate that the extended MALT model can explain the z_p dependence of F_p for various intruder shapes by using V_p and S_p directly. In addition, the analysis results in Sec. 3.4 indicate that differences in the intruder shape have little effect on the prediction accuracy of the model. Previous studies have investigated F_p in columns with varying horizontal cross-sectional geometries, as well as triangular pyramids and hemispheres with circular cross sections and varying Θ [8, 10, 12, 31, 35, 49, 50]. In contrast, we examine the applicability of the model to cases where horizontal cross-sectional geometry, tip shape, and dry or cohesive conditions are varied simultaneously. As a result, the model can estimate F_p even when these factors simultaneously affect. Furthermore, $f(\Theta)$, which was incorporated into the model as a correction factor derived from simulation results using cones, is found to be applicable to other horizontal cross-sectional geometries as well. This finding supports the mechanism of F_p variation due to Θ discussed in our previous studies [35, 49], suggesting that the stagnant zone effectively acts as an intruder.

Though we examine the applicability of the model for various intruder shapes, these shapes are limited to the axisymmetry with triangular cross sections in vertical. Mishra et al. [12], Bergmann and Berry [13], Patino-Ramirez and O'Sullivan [18] have reported that asymmetric intruders and streamlined tip shapes (e.g., elliptical, parabolic) can reduce F_p more than axisymmetric straight tips. Such investigations are crucial for optimizing the design of locomotion and excavating machinery on soil surfaces [3, 7, 16, 17, 24, 56], and for applying the model to the morphology of organisms living in sandy environments [12, 13, 15]. Therefore, future works include evaluating and extending the model to F_p for asymmetrical shapes and streamlined tip shapes.

4.2 Granular type

In this study, the values of K_ϕ and K_c for each granular type are determined based on the failure modes identified from strain fields in granular layer during intruder penetration. As shown in Figs. 6 and 9, K_ϕ and K_c adjusted from the failure mode are quantitatively consistent with the values estimated from the simulation. It has been demonstrated to be effective from a practical perspective for estimating bearing capacity in geotechnical engineering [28, 43]. In addition, the results of ANOVA also indicate that the granular type has a significant impact on the prediction accuracy of the model. Thus, the modification according to failure mode is considered effective for more accurate estimation of F_p. Meanwhile, although previous research focusing on dynamic penetration phenomena in granular materials [4, 32, 41] have examined the influence of various factors on F_p, little attention has been paid to the failure modes. This study, which highlights the influence of failure modes on F_p, is expected to contribute to the future development of more accurate model.

Table 6 ANOVA results for $|k-1|$ show sum of squares (Sum Sq), degrees of freedom (df), F-value, p value, and partial eta-squared (η_p^2) for each factor

Factor	Sum Sq	df	F-value	p value	η_p^2
Intruder Shape	0.004558	2.0	0.195505	0.823365	0.0117
Cohesion	0.001716	1.0	0.147203	0.703683	0.0044
Granular Type	0.190434	3.0	5.445086	0.003737	0.3311
Interface Friction	0.125140	4.0	2.683600	0.048437	0.2454
Granular Type : Interface Friction	0.605229	12.0	4.326332	0.000404	0.6114
Residual	0.384709	33.0			

Table 7 Summary of extended MALT model for each failure mode

Failure mode	General failure	Punching
base model	Eq. (4)	
penetrated intruder volume V_p	Eq. (5) for Cone, SP, and TP	
penetrated intruder area S_p	Eq. (6) for Cone, SP, and TP	
coefficients K_ϕ, K_c	Eq. (7)	Eq. (14)
model cohesive stress C'	$C' = C$	$C' = \psi \frac{C}{\mu_{gg}}$
interface friction effect	Eq. (15)	

As a future direction, it is essential to investigate the influence of ψ on F_p and incorporate its effects into the model. In this study, simulations are conducted under a constant value of $\psi = 0.6$, and failure modes are classified based on granular types. However, when ψ differs, general shear failure may occur for small ϕ, while punching failure may arise for large ϕ. Additionally, Aguilar and Goldman [4], Feng et al. [32] have reported that F_p does not suddenly transit between modes based on ψ but rather increases proportionally with ψ. Therefore, exploring the relationship between F_p and ψ and discussing its effects will improve the accuracy of F_p estimation using the model.

4.3 Bulk cohesive stress

As shown in Fig. 7, the values of C' in the model are expressed using DEM parameters as $C' = \psi \frac{C}{\mu_{gg}}$ for punching (granular types A and B) and $C' = C$ for general failure (granular types C and D). Here, we discuss the differences in the definition of C' based on DEM parameters from a physical perspective according to the failure modes. In the punching mode, shear bands do not develop, and F_p is primarily generated within the stagnant zone. In this situation, it is reasonable to assume that F_p arises from vertical forces acting on the stagnant zone. Moreover, forces in granular layers propagate through force chains, which are spatially heterogeneous [21, 22, 25, 36]. In consequence, C' is also considered to be proportional to ψ. Based on these assumptions, C' in the punching is considered as $C' = \psi \frac{C}{\mu_{gg}}$, defined as the normal component of the cohesive stress between particles multiplied by ψ. In the general failure mode, the majority of F_p is considered to arise from shear bands. Assuming that tangential forces primarily occur between particles within the shear band, C' in the general failure can be calculated as $C' = C$. Moreover, we confirm that this modification of C' does not affect the results of our previous studies [49]. This is because although the modification increases the value of C', the consideration of the failure mode reduces K_c, resulting in minimal change in F_p. Thereby, this result supports the validity of C' defined according to the failure mode in other conditions than this study.

Clarifying the relationship between C and C' is important for the microscopic mechanical interpretation of cohesive granular materials. This may lead to improve the applicability of results from elemental tests such as cone penetration, fall cone, and triaxial compression, as well as standardization of the setting of interparticle cohesion parameters in particle simulations. Although previous studies have discussed various methods for determining simulation parameters [56–58], few studies have established the relationship between the model or the actual measured soil cohesive stress and the parameters. Determining how to set simulation parameters remains a challenging problem for many researchers and engineers. For such applications, it is required in the future to investigate whether the actual cohesive stress measured in various elemental tests can be accurately explained by the proposed relationships. It is also necessary to verify the reliability and interpretation of the ANOVA results, which suggest that cohesion has little effect on the predictive accuracy of the model. In addition, as shown in Fig. 7, estimated C' especially for granular types C and D have large error bars independent of μ_{og}. This suggests that the value of C' (or K_c) varies depending on Θ. Thus, it may be necessary to correct for Θ in relation to the cohesion-derived force in the model.

4.4 Interface friction

By introducing Eq. (15) for K_ϕ and K_c in the extended MALT model, we examine how these coefficients depend on μ_{og}. Figure 9 compares the K_ϕ and K_c estimated from simulations with varying μ_{og} to those calculated in Table 3 and Eq. (15). The model shows a quantitative agreement with the simulation results although some discrepancies are observed. The effect of interface friction has been investigated and widely recognized [21, 27, 28, 43, 50]. In addition, the results of ANOVA also indicate that the interface friction has a significant impact on the prediction accuracy of the model. However, as mentioned by Xi et al. [52], this effect is often ignored in models for estimating F_p. Even in recently developed models, such as the RFT and MALT, hardly consider the effect of interface friction. In contrast, we explicitly demonstrate the μ_{og} dependence on K_ϕ and K_c and indicate its applicability across multiple granular types. As a result, the extended MALT model accounts for the interface friction, enabling more accurate estimations of F_p.

The above discussion suggests that F_p varies with μ_{og}, even for the same granular type. At first glance, this may seem troublesome, as it requires careful consideration of μ_{og} when setting simulation parameters. However, Fig. 9 shows that K_ϕ and K_c rapidly saturate to the values calculated by the model when $\mu_{og} > 0$, even though they are reduced to half their values when $\mu_{og} = 0$. Therefore, when setting DEM parameters using F_p derived from the model, assigning μ_{og} a nonzero value, such as half the value of $\tan\phi$, eliminates the need to explicitly account for the interface friction.

5 Conclusion

In this study, we investigated the effects of intruder shape, granular type (ϕ), interparticle cohesion stress, and interface friction (μ_{og}) on F_p through DEM simulations. Based on these results, we examined the applicability of the extended MALT. From linear regression of the model and simulation results, though R^2 showed a high value, k varied depending on the simulation conditions. Moreover, the prediction accuracy of the model was evaluated by $|k-1|$, and it was $|k-1| = 0.486 \pm 0.521$. Therefore, to improve the prediction accuracy of the model, we considered modifying the model parameters K_ϕ, K_c, and C' based on the failure mode estimated from the $\dot{\gamma}$ distribution and introducing the effect of interface friction to the model. As a result, we obtained the following four key findings:

1. The effect of intruder shape on F_p can be explained by incorporating V_p and S_p into the extended MALT model.
2. The failure modes of the granular layer during intruder penetration transition between punching and general failure depending on ϕ. Consequently, the coefficients K_ϕ and K_c must be adjusted to correspond to the specific failure mode. These values calculated by Eq. (7) should be applied for general failure, whereas those calculated by Eq. (14) should be used for punching.
3. The value of C' also varies according to the failure mode. C' is defined using DEM parameters as $C' = C$ for general failure and $C' = \psi \frac{C}{\mu_{gg}}$ for punching. These definitions arise from the difference in the primary cohesive stress contributing to F_p depending on the failure mode.
4. The effect of μ_{og} on F_p is observed in both dry and cohesive granular layers. To incorporate this effect into the model, we introduce Eq. (15), which accounts for the influence of μ_{og} and ϕ on K_ϕ and K_c.

Based on these findings, the parameters used in the extended MALT model for each failure mode are summarized in Table 7. By following Table 7, the modified model could more accurately predict F_p than before under various conditions. Specifically, $|k-1| = 0.208 \pm 0.155$, improved over the previous model. Furthermore, from η_p^2 calculated in ANOVA, the mainly changed factors in the modified model, granular type and interface friction (and their cross-term), had a significant impact on the prediction accuracy of the model. Therefore, this study contributes the development of more accurate predictive model and offers a comprehensive understanding of the key factors influencing F_p.

Acknowledgements The authors would like to acknowledge the financial support from Komatsu Ltd. This work was supported by JSPS KAKENHI Grant Number JP24H00196.

Funding Open Access funding provided by The University of Osaka.

Data Availability All data in this study are available from the corresponding author on reasonable request.

Declarations

Conflict of interest The authors declare that there is no conflict of interest.

References

1. Tsuji T, Nakagawa Y, Matsumoto N, Kadono Y, Takayama T, Tanaka T (2012) 3-D DEM simulation of cohesive soil-pushing behavior by bulldozer blade. J Terramech 49(1):37–47
2. Li C, Zhang T, Goldman DI (2013) A terradynamics of legged locomotion on granular media. Science 339(6126):1408–1412
3. Obermayr M, Vrettos C, Eberhard P, Däuwel T (2014) A discrete element model and its experimental validation for the prediction of draft forces in cohesive soil. J Terramech 53:93–104
4. Aguilar J, Goldman DI (2015) Robophysical study of jumping dynamics on granular media. Nat Phys 12(3):278–283
5. Miyai S, Kobayakawa M, Tsuji T, Tanaka T (2019) Influence of particle size on vertical plate penetration into dense cohesionless granular materials (large-scale DEM simulation using real particle size). Granular Matter 21(4):105
6. Kobayakawa M, Miyai S, Tsuji T, Tanaka T (2020) Interaction between dry granular materials and an inclined plate (comparison between large-scale DEM simulation and three-dimensional wedge model). J Terramech 90:3–10
7. Servin M, Berglund T, Nystedt S (2021) A multiscale model of terrain dynamics for real-time earthmoving simulation. Adv Model Simul Eng Sci 8(1):1–35
8. Hunt OM, O'Hara KB, Chen Y, Martinez A (2023) Numerical and physical modeling of the effect of the cone apex angle on the penetration resistance in coarse-grained soils. Int J Geomech 23(2):04022273
9. Suzuki H, Kawakami H, Kobayashi T, Ozaki S (2023) Extended terramechanics model for machine–soil interaction: Representation of change in the ground shape and property via cellular automata. Soil Tillage Res 226:105578
10. Paume V, Aussillous P, Pouliquen O (2024) Finite size effects during the penetration of objects in a granular medium. Soft Matter 20(1):245–254
11. Fukumoto T, Yamamoto K, Katsura M, Katsuragi H (2024) Energy dissipation of a sphere rolling up a granular slope: slip and deformation of the granular surface. Phys Rev E 109(1–1):014903
12. Mishra AK, Tramacere F, Guarino R, Pugno NM, Mazzolai B (2018) A study on plant root apex morphology as a model for soft robots moving in soil. PLoS ONE 13(6):0197411
13. Bergmann PJ, Berry DS (2021) How head shape and substrate particle size affect fossorial locomotion in lizards. J Exp Biol 224(11):jeb242244
14. Pirrone S, Del Dottore E, Mazzolai B (2022) Historical evolution and new trends for soil-intruder interaction modeling. Bioinspir Biomim 18(1):011001
15. Yuk J, Pandey A, Park L, Bemis WE, Jung S (2024) Effect of skull morphology on fox snow diving. Proc Natl Acad Sci U S A 121(19):2321179121
16. Martinez A, Dejong J, Akin I, Aleali A, Arson C, Atkinson J, Bandini P, Baser T, Borela R, Boulanger R, Burrall M, Chen Y, Collins C, Cortes D, Dai S, DeJong T, Del Dottore E, Dorgan K, Fragaszy R, Frost JD, Full R, Ghayoomi M, Goldman DI, Gravish N, Guzman IL, Hambleton J, Hawkes E, Helms M, Hu D, Huang L, Huang S, Hunt C, Irschick D, Lin HT, Lingwall B, Marr A, Mazzolai B, McInroe B, Murthy T, O'Hara K, Porter M, Sadek S, Sanchez M, Santamarina C, Shao L, Sharp J, Stuart H, Stutz HH, Summers A, Tao J, Tolley M, Treers L, Turnbull K, Valdes R, Paassen L, Viggiani G, Wilson D, Wu W, Yu X, Zheng J (2022) Bio-inspired geotechnical engineering: principles, current work, opportunities and challenges. Géotechnique 72(8):687–705
17. Martinez A, Chen Y, Anilkumar R (2024) Bio-inspired site characterization – towards soundings with lightweight equipment. arXiv arXiv: physics.geo-ph [physics.geo-ph]
18. Patino-Ramirez F, O'Sullivan C (2024) Optimal tip shape for minimum drag and lift during horizontal penetration in granular media. Acta Geotech 19(1):19–38
19. Michel P, DeMeo FE, Bottke WF (2015) Asteroids IV. University of Arizona Press, Tucson, AZ
20. Katsuragi H (2016) Physics of Soft Impact and Cratering. Springer, Tokyo
21. Zheng H, Wang D, Chen DZ, Wang M, Behringer RP (2018) Intruder friction effects on granular impact dynamics. Phys Rev E 98(3):032904
22. Ballouz R-L, Walsh KJ, Sánchez P, Holsapple KA, Michel P, Scheeres DJ, Zhang Y, Richardson DC, Barnouin OS, Nolan MC, Bierhaus EB, Connolly HC, Schwartz SR, Çelik O, Baba M, Lauretta DS (2021) Modified granular impact force laws for the OSIRIS-REx touchdown on the surface of asteroid (101955) Bennu. Mon Not R Astron Soc 507(4):5087–5105
23. Walsh KJ, Ballouz R-L, Jawin ER, Avdellidou C, Barnouin OS, Bennett CA, Bierhaus EB, Bos BJ, Cambioni S, Connolly HC, Delbo M, DellaGiustina DN, DeMartini J, Emery JP, Golish DR, Haas PC, Hergenrother CW, Ma H, Michel P, Nolan MC, Olds R, Rozitis B, Richardson DC, Rizk B, Ryan AJ, Sánchez P, Scheeres DJ, Schwartz SR, Selznick SH, Zhang Y, Lauretta DS (2022) Near-zero cohesion and loose packing of Bennu's near subsurface revealed by spacecraft contact. Sci Adv 8(27):6229
24. Bagheri H, Jayanetti V, Burch HR, Brenner CE, Bethke BR, Marvi H (2022) Mechanics of bipedal and quadrupedal locomotion on dry and wet granular media. J Field Robot 40(2):161–172
25. Cheng B, Asphaug E, Yu Y, Baoyin H (2023) Measuring the mechanical properties of small body regolith layers using a granular penetrometer. Astrodynamics 7(1):15–29
26. Ruck JG, Wilson CG, Shipley T, Koditschek D, Qian F, Jerolmack D (2024) Downslope weakening of soil revealed by a rapid robotic rheometer. Geophys Res Lett 51(1):e2023GL106468
27. Meyerhof GG (1951) The ultimate bearing capacity of foudations. Géotechnique 2(4):301–332
28. Vesić AS (1973) Analysis of ultimate loads of shallow foundations. J Soil Mech Found Div 99(1):45–73
29. Katsuragi H, Durian DJ (2007) Unified force law for granular impact cratering. Nat Phys 3:420–423
30. Brzinski TA 3rd, Mayor P, Durian DJ (2013) Depth-dependent resistance of granular media to vertical penetration. Phys Rev Lett 111(16):168002
31. Kang W, Feng Y, Liu C, Blumenfeld R (2018) Archimedes' law explains penetration of solids into granular media. Nat Commun 9(1):1101
32. Feng Y, Blumenfeld R, Liu C (2019) Support of modified archimedes' law theory in granular media. Soft Matter 15(14):3008–3017
33. Lee HM, Kim TH, Yoon GH (2024) Analysis of cone-shaped projectile behavior during penetration into granular particles using the discrete element method. Comp Part Mech 11(2):689–703
34. Agarwal S, Goldman DI, Kamrin K (2023) Mechanistic framework for reduced-order models in soft materials: application to three-dimensional granular intrusion. Proc Natl Acad Sci U S A 120(4):2214017120
35. Iikawa N, Katsuragi H (2024) Tip angle dependence for resistive force into dry granular materials at shallow cone penetration. Proceedings of the 21st International and 12th Asia-Pacific Regional Conference of the ISTVS (4927) https://doi.org/10.56884/N04X6LSL, https://easychair.org/publications/preprint/sN6T

36. Cheng B, Yu Y, Baoyin H (2018) Collision-based understanding of the force law in granular impact dynamics. Phys Rev E 98(1–1):012901
37. Koumoto T, Meyerhof GG, Sastry V (1985) Ultimate bearing capacity of axially loaded piles based on three-dimensional analysis. Comput Geotech 1(3):181–194
38. Kobayashi T, Fukagawa R, Matsuura T (2002) Theoretical analysis of CPT and a proposal of an idea for estimating strength parameters. Doboku Gakkai Ronbunshu 2002(708):117–131
39. Roth LK (2021) Constant speed penetration into granular materials: drag forces from the quasistatic to inertial regime. Granular Matter 23(3):54
40. Roth LK, Han E, Jaeger HM (2021) Intrusion into granular media beyond the quasistatic regime. Phys Rev Lett 126(21):218001
41. Yin Y, Huang S, Yu Y, Liu C (2024) Extended application of modified archimedes' law in granular media. Powder Technol 452:120560
42. Mitarai N, Nori F (2006) Wet granular materials. Adv Phys 55(1–2):1–45
43. Terzaghi K (1943) Theoretical Soil Mechanics. Wiley & Sons, Incorporated, John, USA, NY
44. Herminghaus S (2013) Wet Granular Matter: A Truly Complex Fluid. World Scientific, Singapore
45. Dotson B, Sanchez Valencia D, Millwater C, Easter P, Long-Fox J, Britt D, Metzger P (2024) Cohesion and shear strength of compacted lunar and martian regolith simulants. Icarus 411:115943
46. Sharpe SS, Kuckuk R, Goldman DI (2015) Controlled preparation of wet granular media reveals limits to lizard burial ability. Phys Biol 12(4):046009
47. Brzinski TA, Schug J, Mao K, Durian DJ (2015) Penetration depth scaling for impact into wet granular packings. Phys Rev E: Stat, Nonlin, Soft Matter Phys 91(2):022202
48. Zhang X, Zhao H, Cheng H, Wang X, Zhang D (2024) The force and dynamic response of low-velocity projectile impact into 3D dense wet granular media. Powder Technol 434(119309):119309
49. Iikawa N, Katsuragi H (2025) Resistive force modeling for shallow cone penetration into dry and wet granular layers. Acta Geotech 20:1279–1295
50. Liang S, Liu L, Ji S (2021) DEM simulations of resistance of particle to intruders during quasistatic penetrations. Comput Model Eng Sci 128(1):145–160
51. Ye X, Zhang C (2023) Impact granular media for intruders with different geometries: force and rheology. Acta Mech Sin 39(1):722198
52. Xi B, Jiang M, Mo P, Liu X, Yang J (2023) 3D DEM analysis of the bearing behavior of lunar soil simulant under different loading plates. Granul Matter 25(4):1–15
53. Kloss C, Goniva C (2011) LIGGGHTS-open source discrete element simulations of granular materials based on lammps. Supplement Proceed Mater Fabricat Propert Character Model 2:781–788
54. DCS Computing GmbH JL, Corporation S (2016) LIGGGHTS(R)-PUBLIC Documentation, Version 3.X — LIGGGHTS v3.X documentation. https://www.cfdem.com/media/DEM/docu/Manual.html. Accessed: 2025-1-22
55. Jiang M, Shen Z, Wang J (2015) A novel three-dimensional contact model for granulates incorporating rolling and twisting resistances. Comput Geotech 65:147–163
56. Wiberg V, Servin M, Nordfjell T (2021) Discrete element modelling of large soil deformations under heavy vehicles. J Terramech 93:11–21
57. Zhu J, Zou M, Liu Y, Gao K, Su B, Qi Y (2022) Measurement and calibration of DEM parameters of lunar soil simulant. Acta Astronaut 191:169–177
58. Sato N, Ishigami G (2024) Parameter study and identification of DEM modeling for varied sand moisture content based on bulldozing experiment. J Terramech 113–114(100971):100971